LETTER



Virtual-point-based deconvolution for optical-resolution photoacoustic microscopy

Rui Yao¹ | Anthony DiSpirito¹ | Hongje Jang² | Colton Thomas McGarraugh¹ | Van Tu Nguyen¹ | Lingyan Shi² | Junjie Yao¹

Correspondence

Junjie Yao, Department of Biomedical Engineering, Duke University, Durham, NC 27708, USA.

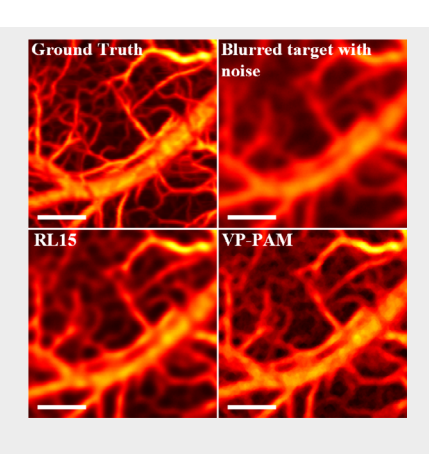
Email: junjie.yao@duke.edu

Funding information

United States National Institutes of Health (NIH), Grant/Award Numbers:
R21EB027981, R21 EB027304, RF1
NS115581, R01 NS111039, R01 EB028143,
R01DK139109; The United States National
Science Foundation (NSF) CAREER,
Grant/Award Number: 2144788; Duke
University Pratt Beyond the Horizon
Grant; Eli Lilly Research Award Program;
Chan Zuckerberg Initiative Grant,
Grant/Award Number: 2020-226178

Abstract

Optical-resolution photoacoustic microscopy (OR-PAM) has been increasingly utilized for in vivo imaging of biological tissues, offering structural, functional, and molecular information. In OR-PAM, it is often necessary to make a trade-off between imaging depth, lateral resolution, field of view, and imaging speed. To improve the lateral resolution without sacrificing other performance metrics, we



developed a virtual-point-based deconvolution algorithm for OR-PAM (VP-PAM). VP-PAM has achieved a resolution improvement ranging from 43% to 62.5% on a single-line target. In addition, it has outperformed Richardson-Lucy deconvolution with 15 iterations in both structural similarity index and peak signal-to-noise ratio on an OR-PAM image of mouse brain vasculature. When applied to an in vivo glass frog image obtained by a deep-penetrating OR-PAM system with compromised lateral resolution, VP-PAM yielded enhanced resolution and contrast with better-resolved microvessels.

KEYWORDS

deconvolution, genetic algorithm, photoacoustic microscopy

1 | INTRODUCTION

Photoacoustic microscopy (PAM) is a major implementation of photoacoustic imaging with balanced spatial resolution, penetration depth, and imaging speed [1, 2]. PAM provides optical absorption contrast for endogenous biological molecules like hemoglobin, fat, and melanin in vivo via the photoacoustic effect. This capability has attracted significant attention for biological and preclinical applications in vascular biology, monitoring brain activities, cancer detection, and more [3–23]. Based on

the relative sizes of optical versus acoustic foci, PAM is categorized into either optical-resolution PAM (OR-PAM) or acoustic-resolution PAM (AR-PAM), both of which usually employ point-by-point scanning of the confocally-aligned optical and acoustic foci. In OR-PAM, the lateral resolution is primarily determined by the optical focusing [24], which is usually more than 10 times tighter than its acoustic focusing. Optical absorbers within the optical focus generate acoustic waves simultaneously, which are detectable by a single-element focused ultrasonic transducer (Figure 1A). Due to the proximity of these optical

¹Department of Biomedical Engineering, Duke University, Durham, North Carolina, USA

²Department of Biomedical Engineering, University of California San Diego, La Jolla, California, USA

18640648, 0, Downloaded from https://onlinelibrary.wiley.com/doi/10.1002/jbio.202400078 by Junjie Yao - Duke University Libraries , Wiley Online Library on [27/06/2024]. See the Terms

ns) on Wiley Online Library for rules of use; OA articles are governed by the applicable Creative Commons

absorbers within the optical focus (much smaller than the acoustic wavelength), they act as a single signal source at each scanning location. The absorbers outside the optical focus contribute little to the final signal (Figure 1B). Hence, an OR-PAM image can be simply approximated as the convolution of the optical focus with the optical absorption distribution of the imaged target. By compromising the lateral resolution, OR-PAM can achieve a deeper penetration, larger field of view, and/or higher imaging speed [1, 12].

Building on the concept of reconstructing images from incoherent virtual point sources, Martinez et al. proposed a deconvolution method, SUPPOSe, to improve the spatial resolution of optical microscopy [25, 26]. SUPPOSe iteratively optimizes the distribution of a large number of virtual points with identical intensities placed on a virtual image, formed by the superposition of these virtual points, until the virtual image convolved with the system's point spread function (PSF) is sufficiently close

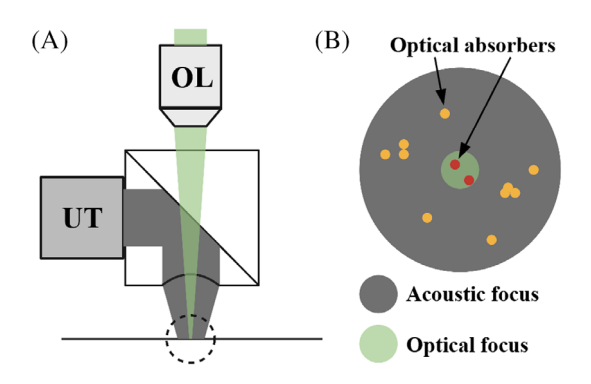


FIGURE 1 Imaging principle of OR-PAM. (A) Schematic of a representative OR-PAM. OL, objective lens; OR-PAM, optical-resolution photoacoustic microscopy; UT, ultrasonic transducer. (B) Cross-sectional view of the focal region circled in (A). Absorbers within the optical focus contribute the most to the detected signal.

to the original image (Figure 2). Doing so, the spatial resolution of the virtual image can be improved over the original image. Although this method was originally applied to optical microscope images, we expect it is also applicable for OR-PAM. A similar approach, Adambased pointillism deconvolution (A-PoD) [27], replaces the genetic algorithm in SUPPOSe with an Adam optimizer. A-PoD uses pixel-level image gradients to individually adjust each virtual point and therefore achieves a faster convergence with improved signal localization. Inspired by both SUPPOSe and A-PoD, we developed a virtual-point-based deconvolution method for OR-PAM (VP-PAM). VP-PAM integrates a novel genetic algorithm that leverages a pixel-level loss function alongside smoothness regularization. The loss for each pixel location is calculated individually without integrating across the image. The new genetic algorithm is designed to improve the performance of VP-based deconvolution techniques on OR-PAM images, which are characterized by a mix of high-frequency and low-frequency components. Since VP-PAM is based on a genetic algorithm, the terms "loss" and "fitness" will be used interchangeably throughout this letter.

2 | METHODS

2.1 | Description of VP-PAM

The fitness score F for pixel (i,j) on the virtual image \widehat{R} can be expressed as a function of the raw image S, the point spread function PSF, and the regularization term ϕ :

$$F_{ij} = \left[S_{ij} - \left(PSF * \widehat{R} \right)_{ij} \right] - \lambda \phi_{ij} \tag{1}$$

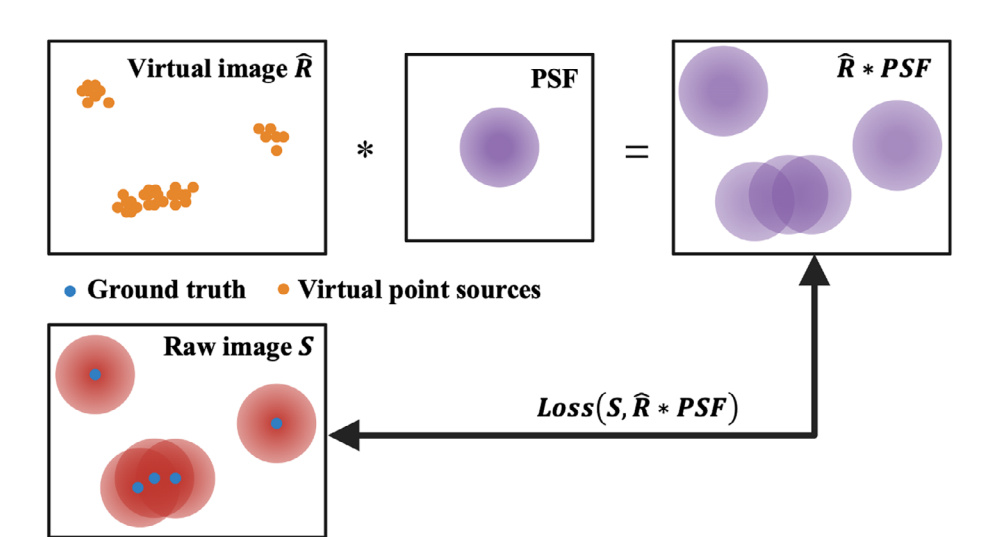


FIGURE 2 Optimization of VP-based deconvolution algorithms. The loss between the raw image S and the estimated virtual image \hat{R} convolved with a known PSF is updated for each iteration. \hat{R} should resemble the ground truth if the loss is small enough. PSF, point spread function; VP, virtual-point.

where * denotes convolution and λ is the regularization coefficient. We enforced the smoothness constraint by implementing a modified local mean method:

$$\phi_{ij} = \beta \left(\widehat{R}_{ij} - u_{ij} \right) + (1 - \beta) \left(\widehat{R}_{ij} - v_{ij} \right)$$
 (2)

where u_{ii} is the mean of the middle five pixel intensities after sorting the 3×3 grid intensities centered at pixel (i,j), and v_{ij} is the average of the two intensities closest to the grid's central intensity. The term $(\widehat{R}_{ii} - v_{ii})$ preserves edges by modulating the penalty on edge regions, whereas $(\widehat{R}_{ij} - u_{ij})$ is primarily used for noise reduction and ensuring image smoothness. Parameter β ($0 \le \beta \le 1$) modulates each term's impact on the regularization score. For a $M \times N$ image S, the total number of virtual points K and the virtual point intensity α follows $K = \sum_{i=1}^{M} \sum_{j=1}^{N} S_{ij}/\alpha$, with either K or α set by the user. In VP-PAM, each virtual point is considered as an individual within a K-sized population. Each individual possesses two genes: the (x,y) coordinates on image \widehat{R} . Individuals with the same genes are identical and therefore possess the same fitness. If we denote the fitness of individual k with genes (x^k, y^k) as F^k , the goal of this optimization problem is to adjust the genes of each individual to minimize the absolute fitness: $x_{optim}^k, y_{optim}^k = \underset{\mathbf{x}^k, \mathbf{y}^k}{\operatorname{argmin}} (\left|F^k\right|), \forall k \in [1, K].$

Figure 3 describes the framework of the genetic algorithm used in VP-PAM. The optimization process depends on the ranking of individual fitness scores. In each generation, individuals with higher fitness scores are more likely to survive and reproduce, propagating their genetic traits to the next generation. On the contrary, those with lower fitness scores are more likely to be discarded and have a reduced chance for reproduction. To keep the population size consistent, the algorithm calculates the requisite number of offspring from the current parent pool, allowing for the possibility of a single parent individual to produce multiple children within one generation. In addition, it is critical to retain the sign of the fitness score from Equation 1 for accurate fitness ranking. For example, with a small regularization term ϕ_{ii} , a more positive F_{ij} indicates the need for additional virtual points at position (i,j), while a more negative F_{ii} indicates that the number of virtual points at that position should be reduced. In practice, the regularization term described in Equation 2 is often nonnegligible: it penalizes the pixel regions with excessively high intensities relative to their neighbors and rewards

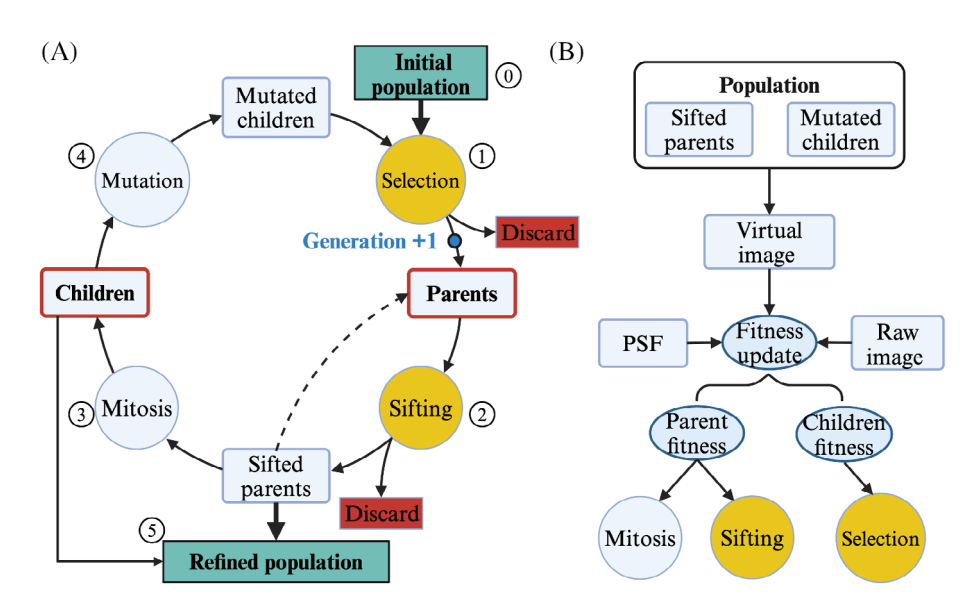


FIGURE 3 Principle of VP-PAM. (A) Schematic of the genetic algorithm implemented in VP-PAM. *Step 0*: Virtual points are randomly spread over a virtual image and form the initial children population. *Step 1*: Children with positive fitness scores are selected and become parents for the new generation, while the rest are discarded. *Step 2*: Low fitness parents are randomly discarded. The sifted parents survive and join the parent population of the next generation. *Step 3*: Sifted parents produce children in a mitosis-like manner—new children are randomly generated within the 3 × 3 pixel Moore neighborhood. Higher fitness parents are likely to produce more children in each generation. *Step 4*: A small portion of children undergo mutation—small, random perturbations are applied to their genes. *Step 5*: Repeat *Steps 1–4* until the maximum number of generations is reached. The final population consists of the sifted parents and the children of the last generation. (B) General workflow showing how the fitness score is updated and utilized. The population size stays the same. VP-PAM, virtual-point-based deconvolution method for OR-PAM.

8640648, 0, Downloaded from https://onlinelibrary.wiley.com/doi/10.1002/jbio.202400078 by Junjie Yao - Duke University Libraries

, Wiley Online Library on [27/06/2024]. See the Terms

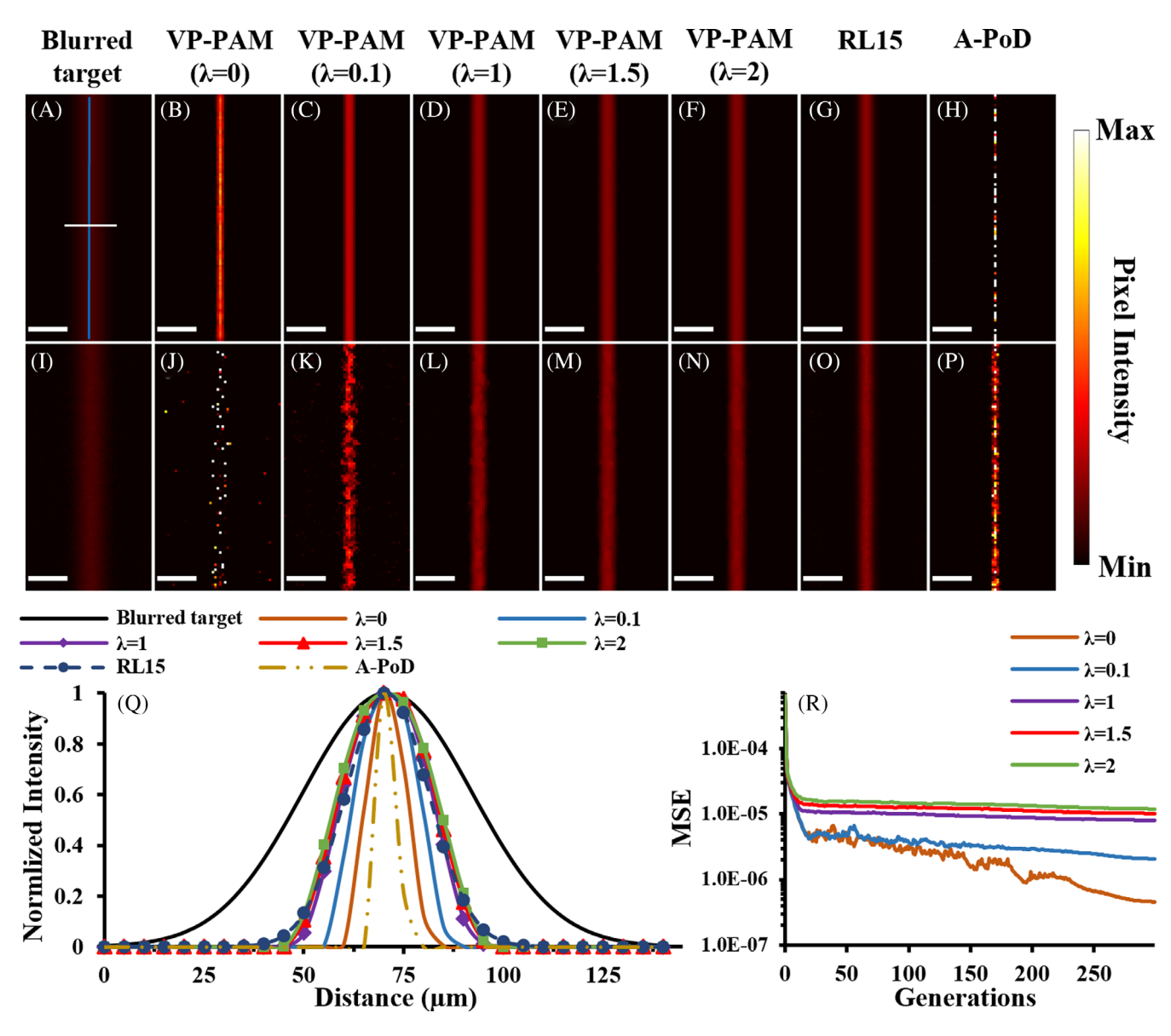
governed by the applicable Creative

JOURNAL OF 4 of 9 dimmer ones. The magnitude of the regularization term ϕ_{ii} remains minimal only if the corresponding region is inherently smooth. 2.2 **Implementation details**

The VP-PAM algorithm employed in this study was developed using Python 3.10.12. For acceleration, the implementation leveraged TensorFlow 2.15.0 on an Nvidia V100-16GB GPU, courtesy of Google Colab's computing resources.

RESULTS AND DISCUSSION

To evaluate the performance of VP-PAM, we began with a binary image of a single-pixel-thick (5 μm) vertical line. This image was first blurred by a factor of 10 using a Gaussian PSF (Figure 4A). We experimented with five different regularization coefficients λ (0, 0.1, 1, 1.5, 2) to deblur the synthesized target. Each deblurring process involved 300 generations and approximately 3.3×10^5 virtual points. The resultant deblurred VP-PAM images (Figure 4B-F) had an FWHM of 12.5, 18.75, 26.0, 27.0,



Resolution enhancement on a synthetic single-line target by various methods. (A) Noise-free blurred single-line target. The blue line represents the ground truth. (B–F) Deblurred VP-PAM results from (A) with $\lambda = 0, 0.1, 1, 1.5, \text{ and } 2, \text{ respectively. (G, H) Deblurred}$ results from (A) using RL15 and A-PoD, respectively. (I) Blurred target with added noise. (J-N) Deblurred VP-PAM results from (I) with different λ values. (O-P) Deblurred results from (I) using RL15 and VP-PAM, respectively. (Q) Line profiles of (B)-(H) along the white line in (A). (R) Evolutions of mean squared error (MSE) of (B)-(F). Scale bar: 75 µm. VP-PAM, virtual-point-based deconvolution method for OR-PAM. RL15, Richardson-Lucy deconvolution with 15 iterations. A-PoD, Adam-based Pointillism deconvolution.

and 28.5 µm, respectively (Figure 40), translating to a resolution improvement of approximately 75%, 62.5%, 48%, 46%, and 43%. Figure 4R shows the mean squared error (MSE) progression for Figure 4B-F, with the lowest final MSE observed at $\lambda = 0$. However, we noted less fluctuation in MSE with larger λ . We then added Gaussian white noise (standard deviation = 0.004, grayscale) to the blurred target, resulting in a final signal-to-noise ratio of 14.57 dB (Figure 4I). Table 1 presents the structural similarity index (SSIM) and peak signal-to-noise ratio (PSNR) of each deblurred image (Figure 4J-N). Among the tested λ values, $\lambda = 0.1$ (Figure 4K) resulted in the highest SSIM and PSNR. λ values of 1, 1.5, and 2 resulted in similar performances. Notably, while there was a decrease in SSIM and PSNR, the deblurred images become smoother and more continuous with a larger λ .

We also compared VP-PAM with Richardson-Lucy (RL) deconvolution [28-30] and A-PoD. RL deconvolution is an iterative approach commonly used in astronomy imaging and optical imaging such as fluorescence microscopy. It was derived using maximum likelihood estimate based on the assumption that each pixel in the observed image follows a Poisson distribution with an expected value given by the true image convolved with a known PSF. Although PA images do not strictly involve Poisson noise, several studies have successfully demonstrated the applicability of RL or RL-based algorithms in PAM, typically using 10-30 iterations [31-36]. Here, we selected RL deconvolution with 15 iterations (RL15) to avoid over-sharpening the deblurred features, which is a common issue for RL deconvolution [32], and the over amplification of noise or artifacts. For the noise-free target, RL15 yielded a resolution enhancement of 50% (FWHM = 25 μm), which is comparable to the performance of VP-PAM with $\lambda = 1$. The latter slightly outperformed RL15 in the noisy target in terms of SSIM (0.74 compared to 0.71, see Table 1). For a fair comparison, A-PoD utilized the same number of virtual points, virtual point intensity, and iterations as VP-PAM. A-PoD surpassed both methods by achieving a resolution enhancement of 88% (FWHM = 6 µm) in the noise-free target (Figure 4H). It also achieved the highest SSIM and PSNR in the noisy target (Figure 4P). However, A-PoD's results were much more discontinuous with concentrated hotspots, even for the noise-free target. A possible explanation for this will be provided later.

TABLE 1 SSIM and PSNR of Figure 4J-P.

	VP-PAM						
	$\lambda = 0$	$\lambda = 0.1$	$\pmb{\lambda} = \pmb{1}$	$\lambda = \textbf{1.5}$	$\lambda = 2$	RL15	A-PoD
SSIM	0.69	0.74	0.74	0.73	0.72	0.71	0.90
PSNR	16.37	18.62	18.26	18.19	18.13	18.31	20.39

Abbreviations: PSNR, peak signal-to-noise ratio; SSIM, structural similarity index metric.

The performance of VP-PAM was further demonstrated using a mouse brain vasculature image acquired by our previously reported high-speed OR-PAM system [3] as the ground truth (Figure 5A). The ground truth image has a size of 900-by-1000 pixels with an 8-µm pixel size and was subsequently blurred by a factor of 10 using a Gaussian PSF, followed by the corruption of Gaussian white noise (standard deviation = 0.004, gray scale), as shown in Figure 5B. Because the resolution enhancement by VP-PAM using $\lambda = 1, 1.5$, and 2 varies only slightly and larger λ values yield smoother vessels, we selected $\lambda = 1.5$ to balance image smoothness with resolution enhancement for VP-PAM. Additionally, we introduced ~87 million virtual points for both VP-PAM and A-PoD. The resulting deblurred image from VP-PAM (Figure 5D) achieved an SSIM of 0.82 and a PSNR of 29.93. This performance surpasses RL15, which attained an SSIM of 0.783 and a PSNR of 27.86 (Figure 5C). Interestingly, although RL15 yielded a greater resolution improvement than VP-PAM with $\lambda = 1.5$ on the single-line target in Figure 4, VP-PAM performed better on the complex target (Figure 5F). The advantage of the VP-PAM method over RL15 is also evident in resolving small vessels (Figure 5G). The deblurred image by A-PoD (Figure 5E), however, showed a large dynamic range, deviating significantly from the ground truth. In addition, virtually all small vessels disappeared after A-PoD deblurring. This poor convergence of virtual points likely resulted from A-PoD's optimization mechanism, which uses an Adam optimizer to iteratively update the coordinates of individual virtual points based on the image gradient of the pixel-wise loss. Since virtual points that initially occupy the same location share identical losses and therefore receive identical updates, they form a collective group and are unable to separate during the iteration. In this case, the smallest intensity unit is not a single virtual point but rather a collective of identical virtual points (i.e., the sum of identical individuals at the same pixel location). As a result, structures with intensities below this collective intensity unit (mostly the small vessels) are unlikely to be restored. In addition, virtual points that join a pre-existing collective group tend to receive similar updates as the collective group in subsequent iterations, due to the Adam optimizer's updating rule and the pixel-wise loss. Conversely, VP-PAM does

//onlinelibrary.wiley.com/doi/10.1002/jbio.202400078 by Junjie Yao - Duke University Libraries , Wiley Online Library on [27/06/2024]. See the Term

FIGURE 5 VP-PAM on a mouse brain vasculature image. (A) Ground truth image of mouse brain vasculature. (B) Blurred image. (C-E) Deblurred images using RL15, VP-PAM, and A-PoD, respectively. For better visualization, (E) was clipped between 0 and 1. (F, G) Line profiles of (A)–(E) along the two solid lines, respectively. Note that (E) was plotted using the right y-axis in (F) and (G). Scale bars: 1 mm for the main images and 400 μ m for the insets. VP-PAM, virtual-point-based deconvolution method for OR-PAM. RL15, Richardson-Lucy with 15 iterations. A-PoD, Adam-based Pointillism deconvolution.

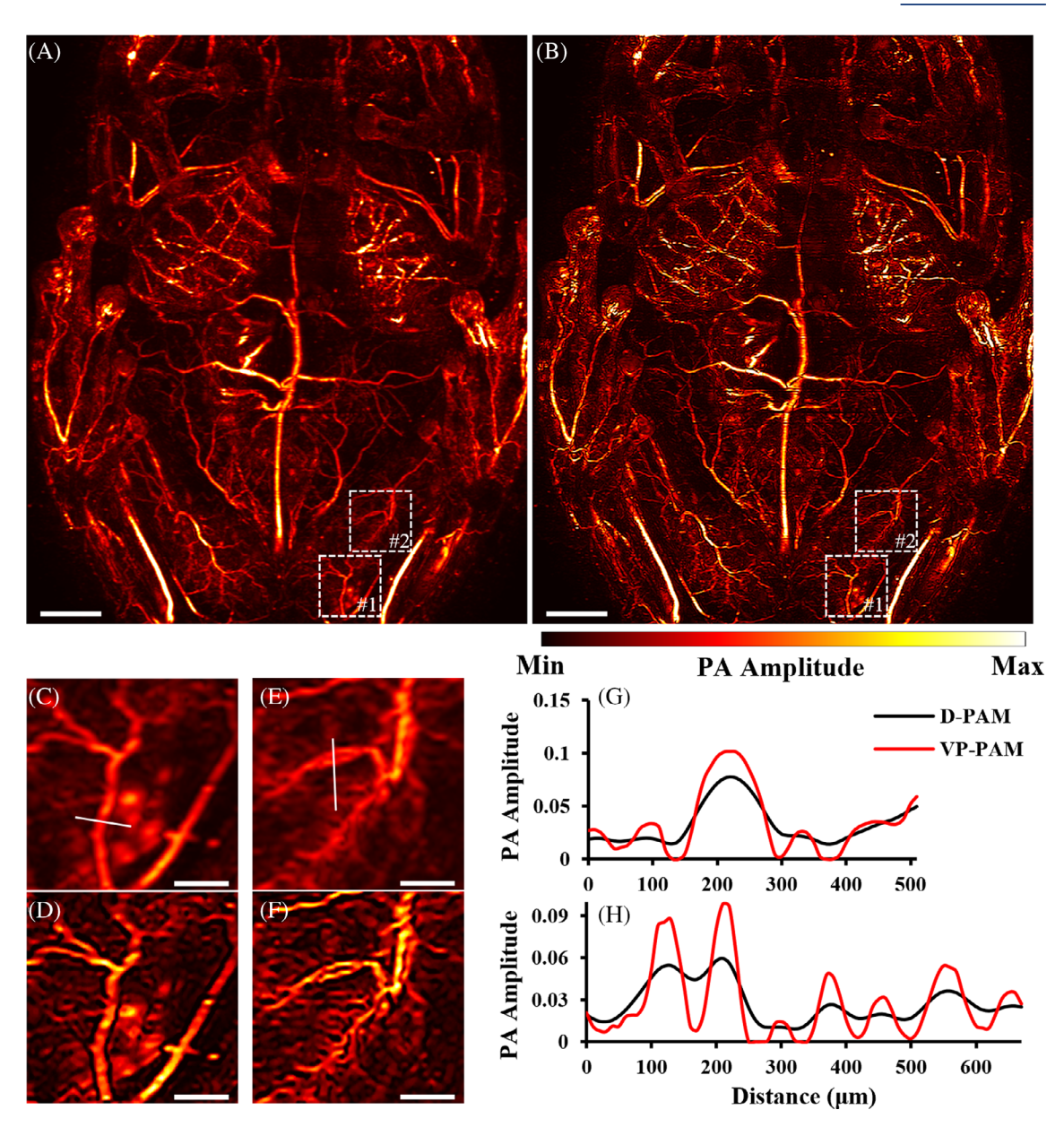


FIGURE 6 VP-PAM on a glassfrog vasculature image. (A) Original D-PAM image of glassfrog vasculature. (B) Deblurred image by VP-PAM. (C, D) Close-up images of the boxed region #1 in (A), (B), respectively. (E, F) Close-up images of the boxed region #2 in (A), (B), respectively. (G) Line profiles of (C) and (D) along the solid line path in (C). (H) Line profiles of (E) and (F) along the solid line path in (E). Scale bars: 2 mm in (A, B), and 500 μ m in (C-F). D-PAM, deep-penetrating PAM; VP-PAM, virtual-point-based deconvolution method for OR-PAM.

not have such issues since it does not adjust the position of existing virtual points; Instead, VP-PAM adds or removes some of the existing ones. The selection process is only applied to the new individuals (children), as described in Figure 3, which helps stabilize the algorithm. The sifting mechanism also randomly removes parent individuals from low-fitness families/collective groups.

Finally, we tested VP-PAM on a 2000×1700 -pixel glassfrog vasculature image obtained by a deep-penetrating PAM (D-PAM) system (Figure 6A) [12]. The system has a lateral resolution of \sim 45 μ m, an imaging

depth of \sim 3 mm, and a depth of focus of \sim 2.5 mm in glassfrogs. While it surpasses traditional OR-PAM systems in terms of imaging depth and depth of focus, its lateral resolution is \sim 10 times worse. It is worth noting that PAM exhibits a depth-dependent PSF that varies significantly between in-focus and out-of-focus regions. The in-focus signals and out-of-focus signals in PAM can be separated based on the acoustically-resolved depths. Since VP-PAM relies on shift-invariant PSF, we specifically selected the in-focus signals where the PSF is assumed to be consistent. For the deblurring process,

approximately 42 million virtual points were utilized in VP-PAM (Figure 6B). VP-PAM (λ =1.5) effectively improved the clarity of the original image, leading to better-resolved small microvessels with improved contrast (Figure 6C–H).

Computation speed is a crucial factor for image deconvolution algorithms. The current implementation of VP-PAM is GPU-accelerated, which processed the images in 10 s for Figure 4, 100 s for Figure 5, and 110 s for Figure 6. Although VP-PAM is approximately 20-fold slower than RL15, it is still much faster than A-PoD, which required \sim 40 min for Figure 5E. The processing time for both A-PoD and VP-PAM is proportional to the total number of virtual points; however, VP-PAM does not need to track and update the position of every single virtual point each iteration, thereby substantially reducing the processing time per iteration. The processing time for VP-PAM depends on the image size as well because of the convolution operation described in Figure 2. With the same setup, the current algorithm can process 1.2×10^8 virtual points for a 900 × 1000 image in about 117 s with 300 generations. It is important to note that although we observed better VP-PAM performance with increasing virtual points, this improvement would eventually reach a plateau. To improve the computation speed, future efforts can focus on reducing the number of virtual points without significantly compromising the performance. One potential approach is to make individual virtual point intensity α as another optimizable parameter, which might vary among virtual points. This adjustment indicates that regions with higher intensity would require fewer virtual points. Another solution is to incorporate an early-stopping mechanism to reduce the total number of iterations. Additionally, the method described in [25, 26] could be employed to determine the optimal α and K.

VP-PAM is designed to minimize a pixel-level loss function within a genetic algorithm framework, optimizing on a pixel-by-pixel basis without integrating the loss across the entire image. The deblurring method used in VP-PAM can potentially be applied to other imaging modalities with shift-invariant PSFs, such as fluorescence microscopy and stimulated Raman spectroscopy. It is worth noting that this pixel-wise approach is not applicable to shifted PSFs, such as those with motion blurring, as the local loss cannot be properly projected to the correct pixel position in the image space.

The optimization in VP-PAM progresses through selection, sifting, and mitosis of virtual points, all of which heavily rely on the individual fitness ranking. Regularization plays a crucial role in these steps, especially in the sifting step, where parent individuals with low fitness scores are eliminated. This makes sifting especially important. In contrast, selection and mitosis are secondary optimization

mechanisms, which also serve to stabilize the algorithm. To avoid model collapse, we adopted a conservative strategy: to select all children with positive fitness scores and permit each parent to produce a specific number of children based on its fitness ranking, rather than restricting the reproduction opportunities to a limited group of parents. Future improvements to VP-PAM's optimization efficiency should therefore focus on refining these three critical steps.

Lastly, to improve smoothness and local texture, a proper local regularization method is necessary. As mentioned previously, the current regularization strategy promotes smoothness by adjusting the local fitness based on the pixel intensity relative to its neighbors. Specifically, if the intensity of a pixel exceeds the average intensity of its neighboring pixels, its fitness is reduced; and vice versa. This adjustment affects high-frequency signal components, such as noise and edges, more significantly because they are less similar to their surroundings. The regularization coefficient λ dictates the extent to which the fitness is affected. As λ decreases, the sensitivity to local smoothness reduces and the pixel-wise loss plays a more important role in local fitness, making edges sharper but also amplifying noise. We observed that local regularization not only dampens noise amplification but also helps maintain a continuous distribution of virtual points, even in a noise-free target. Based on our experimental results, we recommend λ to be greater than 0.1. Currently, the regularization strategy employs a modified local mean method on a 3×3 grid. For future work, one may consider a larger grid to improve noise resistance and/or edge preservation. Unfortunately, due to the pixel-level loss function used in VP-PAM, it is challenging to apply traditional regularization approaches, such as total variation, which involves a summation of regularization scores over the image.

4 | CONCLUSION

In summary, VP-PAM represents a novel deconvolution strategy for deblurring OR-PAM images, which combines a pixel-level loss function with smoothness regularization to improve image texture. VP-PAM has achieved a resolution enhancement ranging from 43% to 62.5% on a single-line target and outperformed both RL deconvolution and A-PoD in restoring more complex images of mouse brain vasculature, although with a slower processing speed than RL deconvolution. In addition, VP-PAM effectively improved the resolution and contrast of an in vivo glass frog image.

ACKNOWLEDGMENTS

Rui Yao would like to thank Dr. Sandra Martínez for useful discussions.

JOURNAL OF

FUNDING INFORMATION

This work was partially sponsored by the United States National Institutes of Health (NIH) grants R21EB027981, R21 EB027304, RF1 NS115581, R01 NS111039, R01 EB028143, R01DK139109; The United States National Science Foundation (NSF) CAREER award 2144788; Duke University Pratt Beyond the Horizon Grant; Eli Lilly Research Award Program; and Chan Zuckerberg Initiative Grant (2020-226178).

CONFLICT OF INTEREST STATEMENT

The authors declare no financial or commercial conflict of interest.

DATA AVAILABILITY STATEMENT

The data that support the findings of this study are available from the corresponding author upon reasonable request.

ORCID

Rui Yao https://orcid.org/0009-0000-3710-7387

REFERENCES

- [1] J. Yao, L. V. Wang, Laser Photonics Rev. 2013, 7, 758.
- [2] L. V. Wang, Nat. Photonics 2009, 3, 503.
- [3] X. Zhu, Q. Huang, A. DiSpirito, T. Vu, Q. Rong, X. Peng, H. Sheng, X. Shen, Q. Zhou, L. Jiang, U. Hoffmann, J. Yao, Light Sci. Appl 2022, 11, 138.
- [4] H. F. Zhang, K. Maslov, M. L. Li, G. Stoica, L. V. Wang, Opt. Express 2006, 14, 9317.
- [5] D. Zhang, W. Wang, X. Zhu, R. Li, W. Liu, M. Chen, T. Vu, L. Jiang, Q. Zhou, C. L. Evans, D. A. Turner, H. Sheng, J. H. Levy, J. Luo, W. Yang, J. Yao, U. Hoffmann, Anesthesiology 2023, 139, 173.
- [6] R. J. Zemp, L. Song, R. Bitton, K. K. Shung, L. V. Wang, Opt. Express 2008, 16, 18551.
- [7] J. Yao, L. V. Wang, Neurophotonics 2014, 1, 11003. https://doi. org/10.1117/1.NPh.1.1.011003
- [8] J. Yao, L. Wang, J.-M. Yang, K. I. Maslov, T. T. W. Wong, L. Li, C.-H. Huang, J. Zou, L. V. Wang, Nat. Methods 2015, 12, 407.
- [9] J. Yao, K. I. Maslov, Y. Zhang, Y. Xia, L. V. Wang, J. Biomed. Opt. 2011, 16, 076003.
- [10] H. Wu, Y. Tang, B. Zhang, P. Klippel, Y. Jing, J. Yao, X. Jiang, IEEE Trans. Biomed. Eng. 2023, 70, 2279.
- [11] Y. Tang, Z. Dong, N. Wang, A. Del Aguila, N. Johnston, T. Vu, C. Ma, Y. Xu, W. Yang, P. Song, J. Yao, ArXiv 2023.

- [12] C. Taboada, J. Delia, M. Chen, C. Ma, X. Peng, X. Zhu, L. Jiang, T. Vu, Q. Zhou, J. Yao, L. O'Connell, S. Johnsen, Science **2022**, 378, 1315.
- [13] K. J. Rowland, J. Yao, L. Wang, C. R. Erwin, K. I. Maslov, L. V. Wang, B. W. Warner, J. Pediatr. Surg. 2012, 47, 1143.
- [14] O. Rong, C. Taboada, A. d. Águila, I. Merutka, N. Jayasundara, Y. Zeng, W. Yang, Q. Zhou, J. Yao, GEN Biotechnol 2023, 2, 435.
- [15] X. Mu, C. Ma, X. Mei, J. Liao, R. Bojar, S. Kuang, Q. Rong, J. Yao, Y. S. Zhang, Photoacoustics 2024, 38, 100610.
- [16] L. Menozzi, W. Yang, W. Feng, J. Yao, Front. Neurosci. 2022, 16, 1055552.
- [17] B. Lan, W. Liu, Y. C. Wang, J. Shi, Y. Li, S. Xu, H. Sheng, Q. Zhou, J. Zou, U. Hoffmann, W. Yang, J. Yao, Biomed. Opt. Express 2018, 9, 4689.
- [18] C. Kim, C. Favazza, L. V. Wang, Chem. Rev. 2010, 110, 2756.
- [19] S. Jiao, M. Jiang, J. Hu, A. Fawzi, Q. Zhou, K. K. Shung, C. A. Puliafito, H. F. Zhang, Opt. Express 2010, 18, 3967.
- [20] S. Hu, L. V. Wang, Front. Neuroenerg. 2010, 2, 10.
- [21] S. Hu, L. V. Wang, J. Biomed. Opt. 2010, 15, 011101.
- [22] S. Y. Emelianov, P. C. Li, M. O'Donnell, Phys. Today 2009, 62, 34.
- [23] P. Beard, Interface Focus 2011, 1, 602.
- [24] K. Maslov, H. F. Zhang, S. Hu, L. V. Wang, Opt. Lett. 2008, 33, 929.
- [25] M. Toscani, S. Martínez, O. Martínez, Single image deconvolution with super-resolution using the SUPPOSe algorithm (SPIE BiOS), SPIE, San Francisco, CA 2019.
- [26] S. Martínez, M. Toscani, O. E. Martínez, J. Microsc. 2019, 275, 51.
- [27] H. Jang, Y. Li, A. A. Fung, P. Bagheri, K. Hoang, D. Skowronska-Krawczyk, X. Chen, J. Y. Wu, B. Bintu, L. Shi, Nat. Methods 2023, 20, 448.
- [28] L. A. Shepp, Y. Vardi, IEEE Trans. Med. Imaging 1982, 1, 113.
- [29] W. H. Richardson, J. Opt. Soc. Am. 1972, 62, 55.
- [30] L. B. Lucy, Astron. J. 1974, 79, 745.
- [31] L. Zhu, L. Li, L. Gao, L. V. Wang, Optica 2014, 1, 217.
- [32] F. Feng, S. Liang, J. Luo, S.-L. Chen, Photoacoustics 2022, 26, 100360.
- [33] F. Feng, S. Liang, S. L. Chen, Biomed. Opt. Express 2022, 13, 1026.
- [34] J. Chen, R. Lin, H. Wang, J. Meng, H. Zheng, L. Song, Opt. Express 2013, 21, 7316.
- [35] D. Cai, Z. Li, Y. Li, Z. Guo, S.-L. Chen, Opt. Express 2017, 25,
- [36] D. Cai, Z. Li, S. L. Chen, Biomed. Opt. Express 2016, 7, 369.

How to cite this article: R. Yao, A. DiSpirito, H. Jang, C. T. McGarraugh, V. T. Nguyen, L. Shi, J. Yao, J. Biophotonics 2024, e202400078. https:// doi.org/10.1002/jbio.202400078